

pubs.acs.org/acscatalysis Research Article

Restructuring of Benzimidazole-Based Copper Complexes during **Electrochemical CO₂ Reduction**

Rafael L. Romano, Maykon L. Souza, Antonio C. Roveda, Jr., Xueru Zhao, Kotaro Sasaki,* and Fabio H. B. Lima*



Cite This: ACS Catal. 2025, 15, 20135-20148



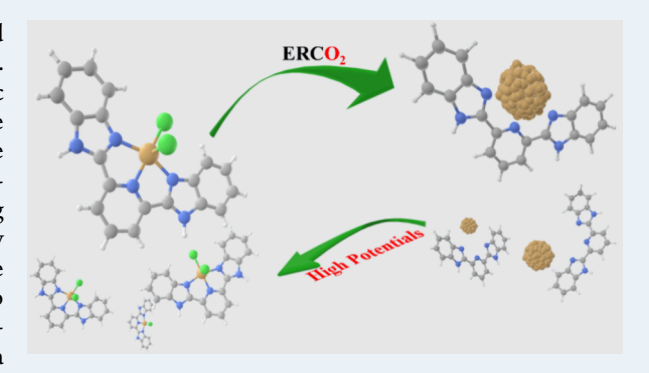
ACCESS I

Metrics & More

Article Recommendations

Supporting Information

ABSTRACT: Copper-based molecular catalysts have been widely used for the electrochemical reduction of carbon dioxide (ERCO₂). However, establishing a correlation between structure and catalytic performance has been challenging due to the dynamic nature of these materials under ERCO2 working conditions. Here, we report on the restructuring of the copper complexes [Cu(bzimpy)Cl₂] and [Cu-(pyrben)₂(NO₃) NO₃ during ERCO₂ in an acidic medium, evidencing its effects on the observed activity, selectivity, and stability. In situ X-ray absorption spectroscopy (XAS) suggested that, at sufficiently negative potentials, the Cu²⁺ centers of both complexes are reduced to undercoordinated Cu⁰ species. Pb underpotential deposition of post-ERCO₂ samples indicated that such Cu⁰ species also present a dominant contribution of the (100) domain, which is in line with the



high Faradaic efficiency toward C₂ products (~45%) shown by both complexes at −1.24 V vs RHE. By combining online electrochemical mass spectrometry, in situ XAS, electron paramagnetic resonance (EPR), and quantitative product analysis, we found that $[Cu(bzimpy)Cl_2]$ exhibits a partially reversible restructuring, regenerating the main complex moiety, $[Cu(bzimpy)]^{2+}$, and its geometry.

KEYWORDS: electrochemical CO₂ reduction, copper complexes, restructuring, in situ XAS, online EC-MS

INTRODUCTION

The increasing levels of carbon dioxide (CO₂) in the atmosphere highlight the urgent need for the development of reliable strategies to reduce its net emissions. Among several approaches developed so far, the electrochemical reduction of carbon dioxide (ERCO₂) stands out as a promising CO₂ utilization technology that enables the production of valuable fuels and chemicals, contributing to the establishment of a carbon-neutral economy. 1-3 However, significant drawbacks for its practical applications lie in the high required overpotentials and poor selectivity, 4-6 which makes the rational design of active, selective, and stable electrocatalysts a key step toward large-scale ERCO2 usage. Due to the unique ability of copper to promote the electrochemical reduction of CO2 to hydrocarbons and alcohols with significant Faradaic efficiencies,^{7,8} copper-based materials have been extensively studied. Particularly, Cu complexes have garnered substantial attention due to their well-defined structures and high CO2 reduction selectivity. 9-15 Efforts have been directed toward understanding the correlation between structure and catalytic performance, but such a task has been challenging, as many of these catalysts undergo restructuring under ERCO2 working conditions. The restructuring processes were found to play a dual effect on the overtime performance, being (a)

related to the formation of catalytically active species, which may take place through changes in Cu oxidation state and/or coordination number, 17,19,20 and (b) involved in several degradation and deactivation mechanisms, such as agglomeration, dissolution, and fragmentation.²¹ Therefore, an in-depth investigation of the restructuring phenomena is essential to comprehend the catalytic properties of a given material.

In situ/operando characterization techniques have been widely used to probe the structural changes of Cu-based electrocatalysts. By using operando X-ray Absorption Spectroscopy (XAS), Sargent and co-workers 11 identified the formation of Cu nanoparticles from molecular Cu-cluster precatalysts during ERCO2 in acidic medium. Besides, the operando Raman measurements revealed that the undercoordinated Cu sites are stabilized through the interaction with the surrounding organic ligands. Ma et al.²⁰ investigated the structural changes of a CTF-Cu (copper-based Covalent Triazine Framework)

September 2, 2025 Received: Revised: October 10, 2025 Accepted: October 13, 2025



catalyst in a 0.3 mol L⁻¹ KCl medium. *In situ/operando* XAS experiments indicated an overtime increase in Cu–Cu coordination number, reaching an approximately constant value of 4.5 after 80 min of electrolysis at –1.45 V vs SHE. In a similar study, Weng et al. ¹⁹ demonstrated that a Cu²⁺-phthalocyanine catalyst experiences restructuring under ERCO₂ conditions, with Cu²⁺ being reduced to nanostructured Cu⁰ species of 2 nm size, which were shown to be highly selective for methane formation. Interestingly, both Ma et al. ²⁰ and Weng et al. ¹⁹ reported evidence of reversible restructuring, in which the initial structures of the catalysts were fully restored after ERCO₂ upon applying a sufficiently positive potential or at open circuit potential conditions.

Despite significant progress in comprehending the structural evolution of Cu-based molecular catalysts under CO_2 reduction working conditions, a clear structure-performance correlation remains elusive. Additionally, aspects of the reversible restructuring process are still under debate, including the conditions (electrochemical and structural) under which the material exhibits such behavior and its effects on the catalyst activity, selectivity, and stability toward CO_2 reduction. These points strongly motivated the present study. Herein, the catalytic properties of two benzimidazole-based copper complexes, $[\mathrm{Cu}(\mathrm{bzimpy})\mathrm{Cl}_2]$ and $[\mathrm{Cu}(\mathrm{pyrben})_2(\mathrm{NO}_3)]\mathrm{NO}_3$ (Figure 1), were evaluated in a CO_2 -saturated 0.1 mol L^{-1}

Figure 1. Molecular structures of the Cu²⁺ complexes considered in this study: (a) [Cu(bzimpy)Cl₂] and (b) [Cu(pyrben)₂(NO₃)]NO₃, where *bzimpy* and *pyrben* refer to the organic ligands 2,6-bis(2-benzimidazolyl)pyridine and 2-(2-pyridyl)benzimidazole, respectively.

 $\rm K_2SO_4$ aqueous solution (pH 4.2). While benzimidazole groups are known to present beneficial effects for the catalyst performance toward $\rm CO_2$ electroreduction, $^{22-26}$ the water insolubility and N-based chelating features of the ligands bzimpy and pyrben (2,6-bis(2-benzimidazolyl)pyridine and 2-(2-pyridyl)benzimidazole, respectively) may contribute to the reversible restructuring of the complexes. In situ XAS, online electrochemical mass spectrometry (EC-MS), electron paramagnetic resonance (EPR), and quantitative product analysis were used to study the restructuring processes and their effects

on the catalytic performance. The results are discussed based on the properties of the ligands *bzimpy* and *pyrben*, and on a comparative study performed with copper carbonate (CuCO₃.Cu(OH)₂), a water-insoluble copper-based material free of organic ligands coordinated to Cu²⁺.

■ RESULTS AND DISCUSSION

Synthesis and Characterization of the Catalysts. $[Cu(bzimpy)Cl_2]$ and $[Cu(pyrben)_2(NO_3)]NO_3$ were synthesized according to the procedures reported by Kirpik et al. and Patel et al., respectively. The former complex was isolated from the purification step as a crystalline solid containing a DMF molecule in the structure, $[Cu(bzimpy)-Cl_2].DMF$. The complete removal of the DMF was carried out by a heat treatment at 220 °C, as shown in thermogravimetric analysis (Figure S1). Elemental analysis (CHN) also demonstrated excellent agreement between experimental and theoretical composition of the final isolated complexes (see Table S1).

According to XRD analysis from literature, ²⁹ [Cu(bzimpy)-Cl₂] is described in a distorted square-pyramidal geometry with a minimal planarity deviation of the *bzimpy* ligand and shorter bond distances at the equatorial plane, Figure S2a. On the other hand, [Cu(pyrben)₂(NO₃)]NO₃ was described as having a distorted trigonal bipyramidal geometry, ²⁸ Figure S2b, which agreed with the observed orthorhombic powdered EPR spectrum, Figure S3b, but did not agree with the axial one in frozen DMF solution, Figure S3d. However, [Cu-(pyrben)₂(NO₃)]NO₃ can also crystallize in a distorted square pyramidal geometry, ³⁰ Figure S2c, which should generate an axial powdered EPR spectrum as observed in frozen solution and discussed next. These pieces of information suggest that [Cu(pyrben)₂(NO₃)]NO₃ must preferably assume a square pyramidal geometry.

EPR spectroscopy was employed to collect additional information regarding the structure and electronic features of the complexes. The powder and frozen solution X-band EPR spectra at liquid nitrogen temperature (77 K) are shown in Figure S3. Figure S4 shows powder spectra recorded at room temperature (298 K) for both nonsupported and carbonsupported complexes. For carbon-supported materials, the only difference is the presence of an extra signal due to localized unpaired electrons in the carbon structure. Table S2 summarizes experimental and simulated EPR parameters from measurements performed with the complexes. The simulations were processed by performing a least-squares fitting using EasySpin software in a Matlab environment. The best-fit output was used to estimate the g and A parameters. The spectra in Figures S3c,d show typical anisotropic signals of copper(II) complexes presenting the four well-defined hyperfine splitting originating from the copper nucleus (I = 3/2)coupling with one unpaired electron (S = 1/2) in a d^9 Cu²⁺ ion (lines = $2 \times N$ nucleus $\times I + 1$). The powdered samples also show typical features with broad signals and no resolved hyperfine lines (lower $A_{||}$) observed for both complexes.^{31,34} The set of g-tensor parameters (-x, -y, -z) with $g_z = g_{||} > g_x = g_y$ = g_{\perp} > g_{e} (g_{e} = 2.0023, free electron g value) suggests a copper(II) center in a distorted structure containing an axial elongation from a square base geometry.³⁵ These features, and the specified set of g values, also suggest the unpaired electron in a $d_{x^2-y^2}$ ground state of the d^9 Cu²⁺ ion complex. Therefore, except for the powder of [Cu(pyrben)₂(NO₃)]NO₃, the listed g values in Table S2 agree with a square pyramidal geometry of

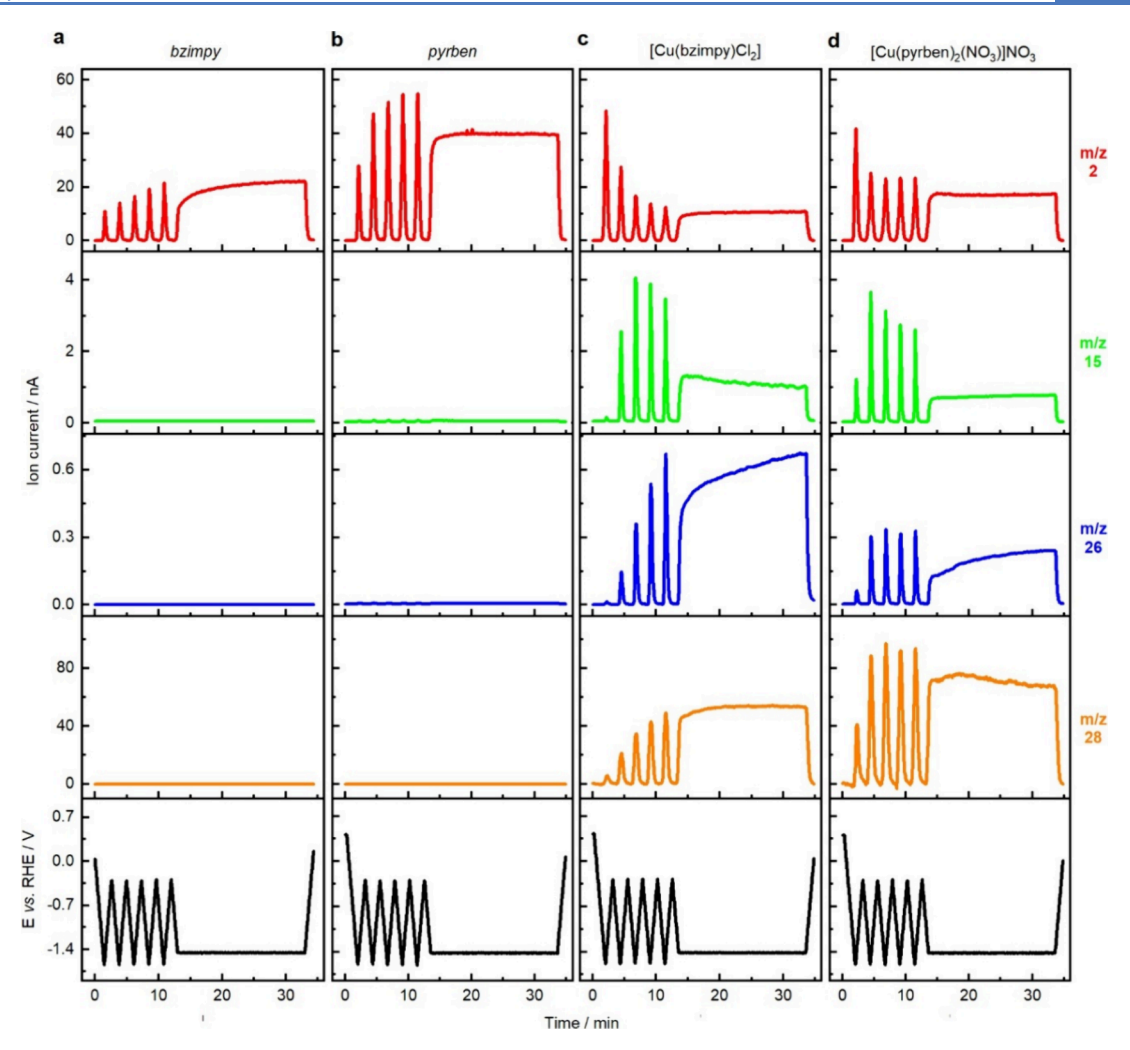


Figure 2. Ion currents for hydrogen (red), methane (green), ethylene (blue) and CO (orange), obtained during EC-MS experiments of cyclic voltammetry (10 mV s⁻¹) and chronoamperometry (at -1.44 V) for the ERCO₂ on (a) *bzimpy*, (b) *pyrben*, (c) [Cu(bzimpy)Cl₂] and (d) [Cu(pyrben)₂(NO₃)]NO₃ in a CO₂-saturated 0.1 mol L⁻¹ K₂SO₄ solution. The electrochemical procedure is shown at the bottom (black).

the complexes, which is in line with XRD and EPR investigations by others and supports the composition, structure, and geometry of the isolated copper complexes in our work. ^{28,29,36,37}

 $[Cu(pyrben)_2(NO_3)]NO_3$, as pointed out earlier, shows some drastic changes to the EPR signal profile when moving from powdered to frozen solution. The evident rhombic spectrum in the powdered sample turned into a well-defined axial spectrum in DMF frozen solution. That behavior appears to result from the geometry change from a less stable geometry at powder (trigonal bipyramidal) to a more stable one (square pyramidal) in solution.

Use of a CO₂-Saturated 0.1 mol L⁻¹ K₂SO₄ Solution as Electrolyte. KHCO₃ solution is a far more commonly used electrolyte for studying CO₂ reduction than K₂SO₄ solution. However, since one of the goals of this study is to investigate the reversible restructuring of copper complexes, a K₂SO₄ solution is a more suitable electrolyte, as discussed below. It is well-known that the stability of species in an electrochemical system depends on the pH and/or the applied potential, as evidenced by the Pourbaix diagrams. In copper-containing systems, different combinations of these variables can lead to the formation of Cu⁰, Cu⁺, Cu²⁺, Cu₂O, CuO, etc.³⁸ Therefore, electrolyte identity plays an important role in the structural

changes (reversible or not) of Cu-based electrocatalysts. Particularly, electrolytes that allow the formation of aqueous Cu species from Cu⁰ at a given electrochemical condition may favor the emergence of reversible restructuring, since this process involves an in situ coordination reaction between Cu ions and the organic ligands on the electrode surface. In a CO₂-saturated 0.1 mol L⁻¹ KHCO₃ solution (pH 6.8), the oxidation of a bulk copper electrode is followed by a passivation process related to the formation of Cu oxide species (Figure S5a).^{39,40} On the other hand, in a CO₂saturated 0.1 mol L⁻¹ K₂SO₄ solution (pH 4.2), Cu⁰ is oxidized to Cu²⁺, which is evidenced by the nearly exponential current increase starting at $\sim 0.5 \text{ V}$ (Figure S5b). Thus, K_2SO_4 is a more suitable choice than KHCO3 to study the reversible restructuring process. As shown in the next sections, many electrochemical procedures employed in this study involve polarizations at high positive potentials (specifically, at 0.96 V) to induce the restructuring of the catalysts by oxidizing the Cu⁰ nanostructures to aqueous Cu²⁺.

The Electrochemical Reduction of CO₂ Catalyzed by Copper Complexes. In the present study, the ERCO₂ was performed in a CO₂-saturated 0.1 mol L⁻¹ K₂SO₄ aqueous solution. At first, control EC-MS measurements were performed to compare the catalytic properties of the Cu

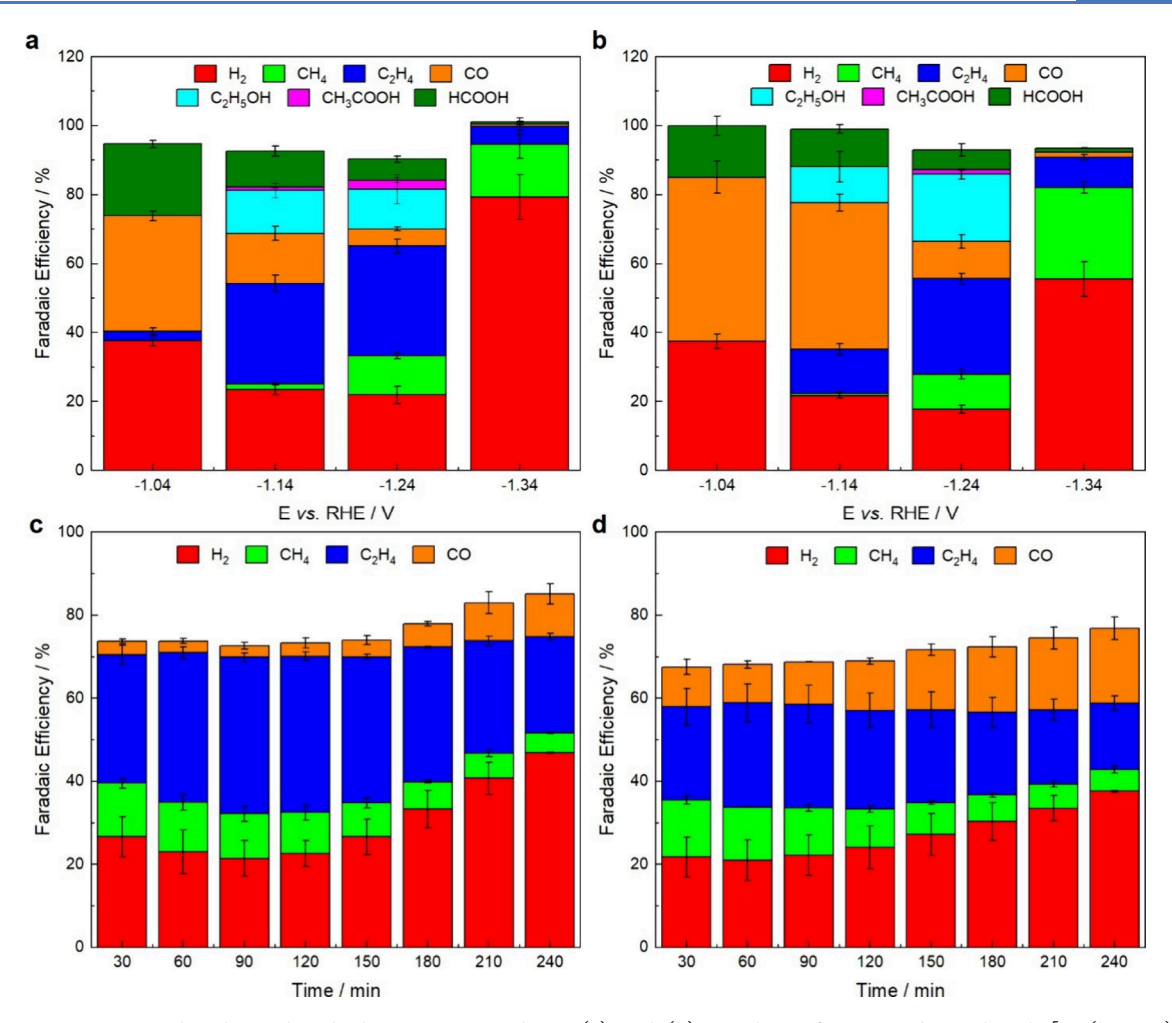


Figure 3. Quantitative results obtained with the copper complexes. (a) and (b) Faradaic efficiencies obtained with $[Cu(bzimpy)Cl_2]$ and $[Cu(pyrben)_2(NO_3)]NO_3$, respectively, at four representative potentials. (c) and (d) Faradaic efficiencies obtained during stability measurements at -1.24 V, performed with electrodes formed by $[Cu(bzimpy)Cl_2]$ and $[Cu(pyrben)_2(NO_3)]NO_3$, respectively.

complexes with those of the support materials and the organic ligands themselves. In a typical online EC-MS experiment, the ion currents of m/z fragments 2 (H₂), 15 (CH₄), 26 (C₂H₄), and 28 (CO) were recorded versus time and applied potentials. Figure 2 and Figure S6 present the results obtained during cyclic voltammetry and chronoamperometry measurements performed with different electrode materials. Experiments were carried out using the setup depicted in Figure S7.

As expected, the electrodes defined as "blanks" (Figures 2a,b, and Figure S6) led to exclusive H₂ formation due to H₂O reduction, evidencing that neither the support materials (carbon paper and Vulcan carbon) nor the ligands (bzimpy and pyrben) are active for CO2 reduction. On the other hand, the electrodes formed by the complexes [Cu(bzimpy)Cl₂] and [Cu(pyrben)₂(NO₃)]NO₃ exhibited activity toward CO₂ and $\mathrm{H}_2\mathrm{O}$ reduction, leading to the formation of H_2 , CO , CH_4 and C₂H₄ (Figures 2c,d). As a common behavior to both complexes, H₂ formation decreases as CO, CH₄ and C₂H₄ formation increase during the potential cycling, revealing a time-dependent activation behavior of the electrodes in the ERCO₂ process. EC-MS analysis was also conducted during a 1.0 mV s⁻¹ cyclic voltammetry measurement to estimate the onset potential of gaseous CO2 reduction products. Here, the onset potential was defined as the potential at which 2% of the maximum ion current (at -1.34 V) is reached. Such an

approach of stating a threshold current to define the onset potential is commonly found in the literature. Figure S8 shows the faradaic current vs potential profile and the ion current vs potential curves for m/z fragments 2, 15, 26, and 28. By comparing the results obtained with [Cu(bzimpy)Cl₂] and [Cu(pyrben)₂(NO₃)]NO₃, no significant differences were observed. For both complexes, H₂ formation was detected at approximately -0.7 V, coinciding with an increasing in faradaic current. CO was the first ERCO₂ product to be detected, showing an onset potential of approximately -0.9 V. Finally, methane and ethylene formation were detected at ~ -1.2 V. The onset potential sequence, H₂ > CO > hydrocarbons, was also observed for other Cu-based materials, $^{42-44}$ and it is in line with mechanistic studies that point out (adsorbed) CO as a key intermediate for hydrocarbons formation.

Based on the results obtained by online EC-MS, four potential values were chosen for product quantification experiments. However, before presenting these results, it is worth discussing the specific configuration of the electrochemical cell used in quantitative measurements (Figure S9). The use of this setup was required because a significant increase in the catholyte pH was detected during $\rm CO_2$ reduction experiments when using the conventional gastight H-cell (cathode and anode separated by a Nafion membrane) filled with a $\rm CO_2$ -saturated 0.1 mol $\rm L^{-1}$ K₂SO₄ solution. This

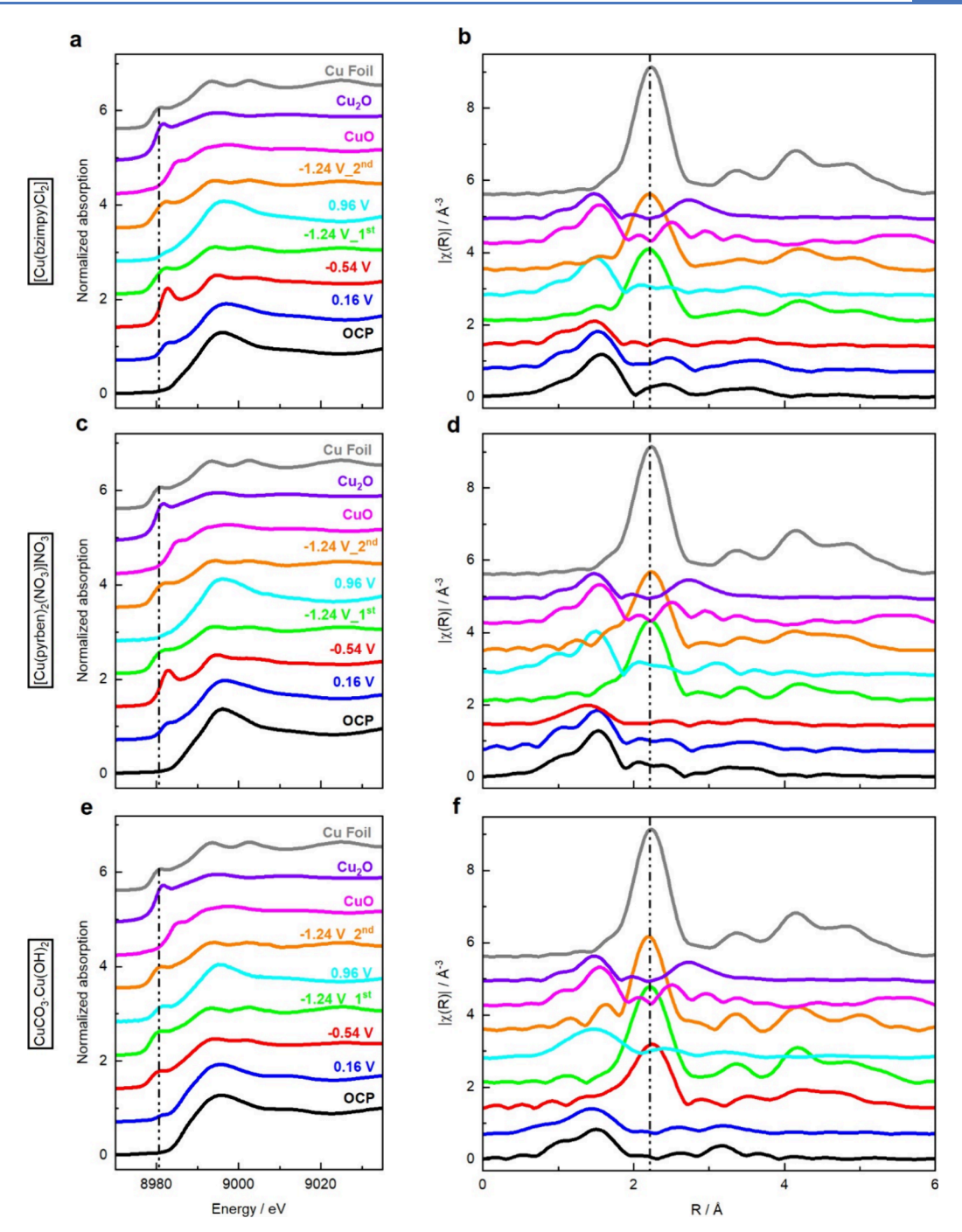


Figure 4. In situ XAS spectra obtained under ERCO₂ conditions. (a) Cu K-edge XANES spectra and (b) Fourier-transformed EXAFS spectra obtained for [Cu(bzimpy)Cl₂]. The corresponding XAS spectra obtained for [Cu(pyrben)₂(NO₃)]NO₃ and CuCO₃·Cu(OH)₂ are depicted in (c), (d) and (e),(f), respectively. The FT-EXAFS signals of Cu₂O and CuO were multiplied by 2 for better visualization.

pH instability, recently reported by Liu et al., 45 is related to the diffusion of K⁺ through the Nafion membrane, competing with H⁺ diffusion. It is well-known that both CO₂ and H₂O reduction lead to OH⁻ formation and, since a CO₂-saturated K₂SO₄ solution is not a buffer, the reduced amount of H⁺ diffusing through the membrane (due to K⁺ competition) results in a pH increase. This problem was solved by modifying the anode compartment of the H-cell (Figure S9). In this configuration, such a compartment is electrolyte-free, and hydrogen gas is oxidized over a Pt/C electrode pressed against a Nafion membrane. H₂ oxidation results in H⁺ formation, which immediately diffuses through the membrane, allowing

the maintenance of the bulk catholyte pH during CO_2 reduction.

To evaluate the selectivity of the catalysts for ERCO₂, product quantification was performed at four representative potentials: -1.04, -1.14, -1.24 and -1.34 V vs RHE. The total electrolysis time was 30 min, but quantification was carried out during the last 20 min of the reaction. Figures 3a,b show the Faradaic Efficiencies (FE) obtained with [Cu-(bzimpy)Cl₂] and [Cu(pyrben)₂(NO₃)]NO₃, respectively. Representative chromatograms are shown in Figure S10.

At -1.04 V, both Cu complexes produce CO and HCOOH as the main CO₂ reduction products, and only [Cu(bzimpy)-

 Cl_2 produces ethylene at quantifiable amounts (FE = 2.7%). As the potential is decreased to -1.14 V, the FE toward H₂ and CO decreases, while the formation of hydrocarbons is favored. Besides, ethanol production begins at this potential. At -1.24V, both complexes become more selective toward ERCO₂ and reach a total FE of ~ 45% toward C2 products. At high negative potential (-1.34 V), CO_2 reduction is suppressed, and H₂ becomes the main reaction product. From the current vs time curves (Figure S11), one observes a nearly exponential increase in current during the first 10 min of electrolysis at all investigated potentials. Such a current profile indicates an activation process, which may be related to the restructuring of the catalysts. By evaluating the product distribution during the first 10 min of electrolysis at -1.24 V (Figure S12), one notes that both complexes exhibit a total FE toward gaseous and liquid products of ~ 55%, suggesting that the charge flowing through the system is partially directed to a process other than the ERCO₂ or the Hydrogen Evolution Reaction (HER), which is probably the reduction of the Cu2+ centers to nanostructured Cu⁰ species. This hypothesis is supported by the in situ XAS results, presented later in this study.

Due to the high current density and enhanced CO₂ reduction selectivity observed at -1.24 V, further investigations were performed at this potential. Stability tests were conducted over a 4-h period, and the distribution of the gaseous products was monitored as a function of time. For [Cu(bzimpy)Cl₂] (Figure 3c), one observes an increase in FE toward ethylene during the first 90 min of electrolysis, reaching a maximum value of 38%. Then, with an increase in time, ERCO₂ is suppressed, and H₂ formation gradually increases, reaching 48% after 4 h. For [Cu(pyrben)₂(NO₃)]NO₃ (Figure 3d), similar trends are observed, but the overtime increase in the FE toward H₂ is less pronounced, reaching 38% after 4 h. From the current vs time curves (Figure S13), one notes that the electrodes exhibit significant deactivation during the electrolysis time, which is possibly related to two main effects: (a) the coalescence of small nanostructures into larger nanoparticles and aggregates (as described in the next section) and (b) the poisoning of the electrode by the electrodeposition of metal impurities from the electrolyte; both effects can also contribute to the enhancement of the HER over ERCO₂. 21,46-48

Probing the Active Sites. Figure S14 shows the Transmission Electron Microscopy (TEM) images of post-CO₂ reduction samples collected after a 30 min electrolysis at −1.24 V. TEM analysis revealed that both complexes form small Cu⁰ nanostructures showing nonuniform distribution, morphology, and size. The Cu⁰ species formed from [Cu(bzimpy)Cl₂] exhibited a size ranging from ~ 2 to ~ 8 nm, while those formed from [Cu(pyrben)₂(NO₃)]NO₃ exhibited a broader size distribution, ranging from ~ 2 to \sim 25 nm. The high-resolution TEM images (Figure S14b,e) evidence the lattice fringes of selected nanoparticles formed from [Cu(bzimpy)Cl₂] and [Cu(pyrben)₂(NO₃)]NO₃, showing interplanar spacing of 0.216 and 0.285 nm, respectively. For longer electrolysis time, the formation of larger nanostructures and aggregates was observed (Figure S15). [Cu(bzimpy)Cl₂] and [Cu(pyrben)₂(NO₃)]NO₃ formed Cu⁰ nanoparticles with size ranging from ~ 3 to ~ 23 nm and ~ 11 to \sim 40 nm, respectively, after 4 h. The agglomeration of smaller structures into larger ones is a common phenomenon for nanocatalysts^{21,46} and may take place through the particle migration and coalescence mechanism.⁴⁹ As a consequence,

changes in product distribution and a decrease in the active surface area can be observed. Thus, this agglomeration process is likely associated with the deactivation shown in Figure S13 and with the progressive enhancement of the HER observed in Figures 3c,d. It is worth mentioning, however, that other common deactivation processes may also occur concurrently. 21,46

Further characterization of the Cu⁰ nanostructures was carried out through Pb underpotential deposition (Pb-UPD) experiments. As a surface-sensitive process, Pb-UPD can provide important information concerning the distribution of crystallographic domains on the electrode surface. 50,51 Additionally, the experimental setup used in this study prevents samples from being exposed to air, avoiding subsequent reconstruction of the structures formed in situ.¹⁷ The lead UPD results, overlapped with the profiles of Cu single crystals, are presented in Figure S16. As expected, each electrode displays unique Pb-UPD profile, with cathodic and anodic processes developing in specific potential windows. By comparing the cathodic features of the CVs presented in Figure S16, one notes that those observed for the complexes overlap with that of Cu(100), suggesting that the Cu⁰ species formed from both [Cu(bzimpy)Cl₂] and [Cu-(pyrben)₂(NO₃)]NO₃ at -1.24 V present a dominant contribution of the (100) domain. This facet is well-known for presenting higher CO2 reduction selectivity toward ethylene formation in KHCO3 medium, which is ascribed to its capability of adsorbing higher amounts of CO and promoting CO dimerization at lower overpotentials compared to the other basal planes.⁴² If the (100) domain exhibits similar properties in a CO₂-saturated K₂SO₄ solution, the results obtained by Pb-UPD are in good agreement with the quantitative GC analysis, since both complexes showed higher selectivity toward ethylene.

Next, to investigate the structural evolution of the copper complexes under ERCO2 conditions, in situ XAS measurements were carried out. Figure 4 shows the results obtained during constant potential electrolysis at different applied potentials. In OCP, the X-ray absorption near edge structure (XANES) spectra of both complexes (Figures 4a,c) show a low-intensity pre-edge peak at \sim 8977 eV, which is assigned to the 1s \rightarrow 3d/4p transition in Cu²⁺ centers. ^{52,53} Such a peak can be clearly seen in Figure S17. At the rising-edge region, the peak related to the 1s \rightarrow 4p + LMCT (Ligand-to-Metal Charge Transfer) transition ⁵² is not well-defined and appears as a broad shoulder centered at ~ 8986 eV. Indeed, these spectra are very different from that of the reference CuO (magenta line), which is expected since the spectrum profile and the edge energy depend not only on the Cu oxidation state but also on the coordination environment of the absorbing atom. 53,54 In the Fourier transform extended X-ray absorption fine structure (FT-EXAFS) spectra (Figures 4b,d), the region related to the Cu-N coordination appears between ~ 0.6 and $\sim 2.1 \text{ Å},^{55}$ showing a main peak centered at $\sim 1.6 \text{ Å}.$

When the applied potential is decreased to 0.16 V, the XANES spectra of both complexes change, with a small peak developing at \sim 8983 eV (Figures 4a,c, blue lines). At -0.54 V (red lines), the intensity of this peak increases, and the global profile of the spectra is drastically modified, indicating changes in Cu oxidation state. In the FT-EXAFS spectra (Figures 4b,d), while no Cu-Cu bond peak is detected (at \sim 2.2 Å), one observes a broadening of the region related to the Cu-N coordination and a decrease in peak intensity compared to the

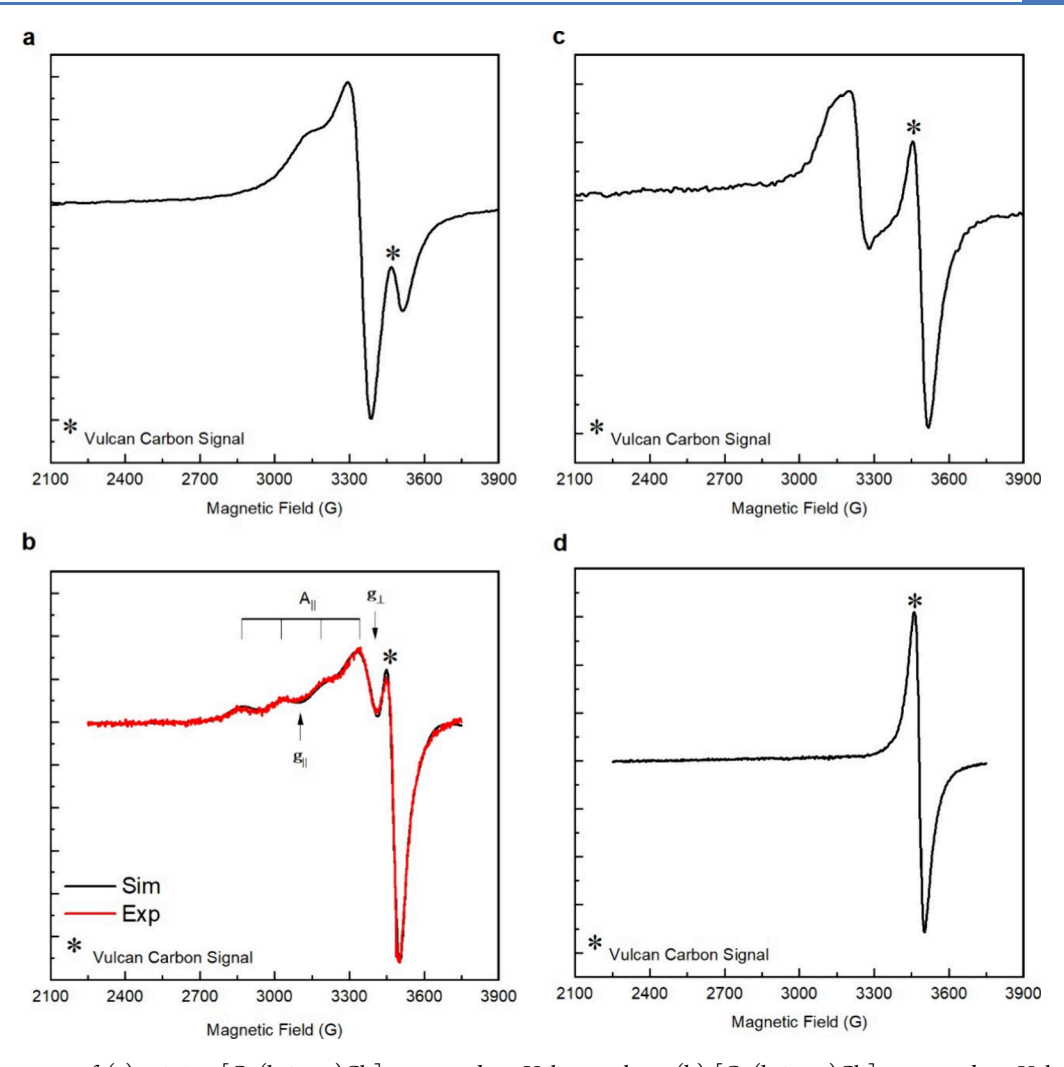


Figure 5. EPR spectra of (a) pristine $[Cu(bzimpy)Cl_2]$ supported on Vulcan carbon; (b) $[Cu(bzimpy)Cl_2]$ supported on Vulcan carbon after anodic polarization; (c) Pristine $[Cu(pyrben)_2(NO_3)]NO_3$ supported on Vulcan carbon; (d) $[Cu(pyrben)_2(NO_3)]NO_3$ supported on Vulcan carbon after anodic polarization. Measurements were performed at room temperature (298 K).

OCP conditions, suggesting that, at -0.54 V, the *in situ* formed structures have the character of molecular Cu species. In contrast, CuCO₃.Cu(OH)₂ exhibits lower electrochemical stability, showing a characteristic Cu-Cu bond peak when the potential is held at -0.54 V (Figure 4f). At -1.24 V (green lines), the XANES spectra of both complexes resemble that of the reference Cu foil, and the FT-EXAFS spectra show a Cu-Cu bond peak centered at ~ 2.2 Å. Note that the intensity of such a peak is smaller than that of the reference Cu foil, suggesting that the catalysts are formed by undercoordinated Cu⁰ species. 56 The fitting analysis of the FT-EXAFS spectra further confirmed the presence of undercoordinated Cu⁰ species at -1.24 V (see Table S3 and Figure S18), which is in line with the high selectivity of both complexes toward C2 products. 56,57 We then hypothesize that the formation of such Cu⁰ species is a ligand-assisted process, ¹¹ so that bzimpy and pyrben play an important role in stabilizing the undercoordinated Cu⁰ sites.

To gain deeper insight into the time-dependent restructuring of the copper complexes, XAS measurements were performed during 90 min of constant potential electrolysis at -1.24 V. From Figures S19a,c, one notes that the XANES spectra of both complexes exhibit significant changes within the first minute of electrolysis, with a prominent peak

developing at ~ 8983 eV. However, the corresponding FT-EXAFS spectra (Figures S19b,d) still exhibit a characteristic Cu-N bond peak and do not show any Cu-Cu bond peak, so that the presence of molecular Cu⁺ (or Cu²⁺) species in this period cannot be ruled out. After 5 min, one observes a significant decrease in the intensity of the Cu-N bond peak and the emergence of a Cu-Cu bond peak, indicating subsequent reduction of the molecular species. After t = 10min, the Cu-Cu bond peak increases, while the Cu-N bond peak slightly changes. Note that the time-evolution of the Cu-Cu bond peak is different for each catalyst: for [Cu(bzimpy)-Cl₂], such a peak gradually increases over time, while for $[Cu(pyrben)_2(NO_3)]NO_3$, it stabilizes after 20 min of electrolysis. In both cases, however, the intensity of the Cu-Cu bond peak is smaller than that of the Cu foil even after 90 min of electrolysis, evidencing the existence of undercoordinated Cu⁰ sites, which also agrees with the high formation of ethylene at t = 90 min (Figure 3).

From the fitting analysis of the time-dependent FT-EXAFS spectra (Table S4), one observes a significant decrease in Cu-N coordination number (CN) from the first to the fifth minute of electrolysis. Thereafter, for [Cu(pyrben)₂(NO₃)]NO₃, the Cu-N CN readily tends to zero, while for [Cu(bzimpy)Cl₂], the Cu-N CN remains around 1 during the first 30 min of

electrolysis. These findings suggest that for the latter complex, there should be small contributions from unreduced copper species to the XAS signal and so to the catalytic activity. While Cu^{2+} is not active in binding CO_2 , a mixture of Cu^{+} and Cu^{0} sites is known to promote C_2 products formation, ⁵⁸ which could also explain the higher selectivity of $[Cu(bzimpy)Cl_2]$ toward C_2 products. The existence of such unreduced Cu^{+} species at -1.24 V may be possible through the interaction of the Cu^{+} centers with the surrounding tridentate ligand bzimpy.

the Cu⁺ centers with the surrounding tridentate ligand bzimpy. Investigation of the Structural Reversibility. TEM and XAS results evidenced that both [Cu(bzimpy)Cl₂] and [Cu(pyrben)₂(NO₃)]NO₃ undergo restructuring at sufficiently negative potentials, forming Cu⁰ nanostructures under CO₂ reduction conditions. To evaluate the reversibility of this process, we applied a specific electrochemical procedure to promote the oxidation of Cu⁰ to Cu²⁺ to induce its coordination to the ligands bzimpy or pyrben. Such a procedure involves an anodic polarization at 0.96 V after a first polarization at -1.24 V. As a control experiment, the same procedure was applied to CuCO₃.Cu(OH)₂, which is free of organic ligands. Figure 4 presents the XAS results of the induced restructuring of the catalysts. In the first polarization at -1.24 V (labeled -1.24 V_1st, green lines), the XAS spectra of both complexes resemble those of the reference copper foil. However, when the potential is increased to 0.96 V (cyan lines), one observes a complete suppression of the Cu⁰ main features and an increase in Cu-N peak in the FT-EXAFS spectra. Correspondingly, the resulting XAS spectra of both complexes resemble those recorded under OCP conditions (black lines), suggesting the formation of molecular Cu²⁺ species at 0.96 V. From the fitting analysis of the FT-EXAFS spectra (Table S3), one observes that [Cu(bzimpy)Cl₂] exhibits a Cu-N CN of 3.4 \pm 0.4, which is close to 3, the expected CN for this complex. On the other hand, [Cu-(pyrben)₂(NO₃)]NO₃ exhibited a Cu-N coordination number of 3.6 \pm 1.3, which is close to 4 (the expected CN), although showing a higher error bar. For CuCO₃.Cu(OH)₂, the XANES spectrum at 0.96 V clearly differs from that obtained at OCP, although the FT-EXAFS spectrum exhibits a complete suppression of the Cu-Cu bond peak and the emergence of a broad feature in the Cu-N bond region. Upon performing a second polarization at −1.24 V (denoted −1.24 V 2nd, orange lines), the resulting XAS spectra of the three catalysts again converge toward that of the metallic Cu foil. Interestingly, by analyzing the corresponding unnormalized XANES spectra (Figure S20), one observes that for CuCO₃.Cu(OH)₂, the absorption intensity significantly drops from the first to the second polarization at -1.24 V. For the complexes, on the other hand, a slight decrease in absorption is observed. These changes in absorption can be related to the amount of Cu2+ that diffuses into the electrolyte during the anodic polarization. The Cu losses were estimated by considering the changes in the edge height (taken as the difference in absorption between pre-edge and postedge lines at 9039 eV)⁵⁹ of the unnormalized XANES spectra recorded at -1.24 V (Figure S20). The calculated changes in edge height were -13.4, -20.8 and -71.7% for $[Cu(bzimpy)Cl_2]$, [Cu(pyrben)₂(NO₃)]NO₃ and CuCO₃.Cu(OH)₂, respectively. These findings strongly suggest that the ligands bzimpy and pyrben play a role in maintaining Cu2+ on the electrode surface after an anodic polarization at 0.96 V. For CuCO₃.Cu(OH)₂, we hypothesize that the Cu⁰ signal recorded during the second

polarization at -1.24 V can be attributed to the electrodeposition of Cu^{2+} on the electrode surface.

EPR spectroscopy was performed on post-ERCO₂ samples to get further insights into the identity of the species generated at 0.96 V. Figures 5a,b present the EPR spectra of the (a) pristine and (b) after anodic polarization [Cu(bzimpy)Cl₂] supported on Vulcan carbon, respectively. The experimental powder spectrum in Figure 5b shows a well-resolved Cu²⁺ hyperfine signal at lower fields $(A_{||})$ and $g_{||} = 2.27$, despite the partial superposition with the paramagnetic signal of the carbon support at the higher field region. That superposition makes it challenging to assign the g_{\perp} (~ 2.05). However, the spectrum in general strongly suggests an axial geometry around the Cu²⁺ ion, since one can notice that $g_{||} > g_{\perp}$. The calculation of the spectrum applying a two-component simulation approach from EasySpin software allowed us to estimate the EPR parameters. The method runs the simulation considering the contribution of both species, Cu²⁺ ions and Vulcan carbon, to the overall signal. The fit presented in Figure 5b (black line) returned the following parameters for the Cu^{2+} ion: $g_z = g_{||} =$ 2.273 ± 0.002 , $g_x = 2.091 \pm 0.05$, and $g_y = 2.021 \pm 0.05$ ($g_{\perp} =$ 2.056), $A_{||} = 535 \pm 9$, $A_x = 63 \pm 117$, and $A_y = 79 \pm 170$. As expected, at the perpendicular axis, there is a high uncertainty regarding the calculation of the g-tensors $(g_x \text{ and } g_y)$ and the respective hyperfine $(A_x \text{ and } A_y)$ as a direct consequence of the superposition of signals. On the other hand, the parallel axis confirmed its well-resolved profile in the spectrum, generating a more confident calculated set of parameters.

Considering that the nuclear hyperfine splitting $(A_{||})$ at $g_{||}$ in copper species is, in most cases, well-resolved and sensitive to the ligand's nature, we can get some insights about the nature of the species in Figure 5b. First, we had to ensure that the signal did not come from a carbon-adsorbed Cu2+ ion (bzimpy free) generated after the anodic dissolution of the copper nanoparticles. Figure S21 shows the EPR spectrum of a powder sample prepared from CuSO₄ supported on Vulcan carbon. The sample was generated after dispersion and ultrasonication of CuSO₄/Vulcan in isopropyl alcohol in the presence of Nafion. The procedure is the same as used to prepare the catalytic inks in this work. No copper(II) EPR signal that resembles the one presented in Figure 5b was observed, but only the one reported for CuSO₄.5H₂O.⁶⁰ Also, it is important to mention that the octahedral ion [Cu- $(H_2O)_6]^{\overline{2}+}$, a possible and simple coordination species formed by Cu²⁺ in aqueous media, is described by a different set of EPR parameters, $g_{||}=2.400$, $g_{\perp}=2.099$, $A_{||}=429$ and $A_{\perp}=36$. The lower values of $A_{||}$ is usually attributed to a system containing weak and less covalent bonds between copper(II) and ligands. 61 Therefore, this result also points to the apparent ability of bzimpy to avoid Cu2+ losses during the anodic polarization. A tridentate N3-type ligand like bzimpy must be efficient in stabilizing the Cu²⁺ and provide some degree of reversibility of the precatalyst complex. That is a reasonable situation, since the moiety [CuN3] could be easily combined with available species (anionic and neutral) originating from the electrolyte (H₂O, OH⁻, SO₄²⁻) or present at the carbon support structure $(-OH, -C = O, -COO^{-})$. In this regard, some insight about the nature of the species from Figure 5b would be taken by comparison to the data from [Cu(bzimpy)-Cl₂] and other copper complexes with tridentate N3-type ligands. Table S5 lists examples of such copper complexes along with their respective EPR parameters. From the data, one can notice that the interaction between the Cu²⁺ and an

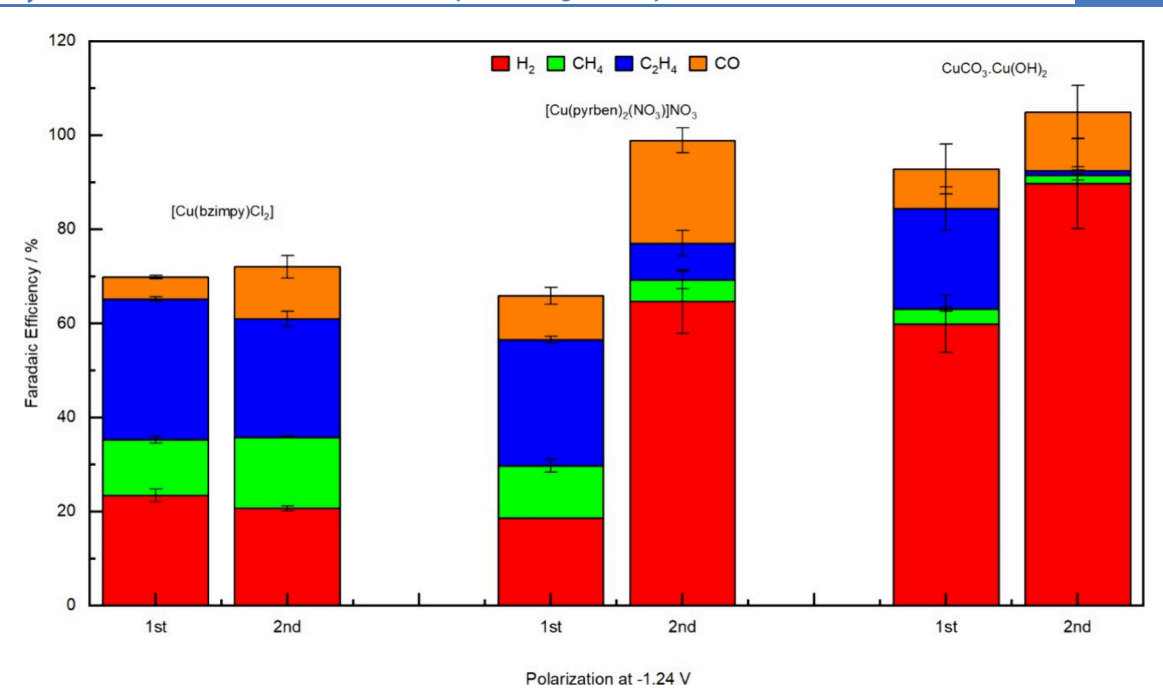


Figure 6. Effect of the anodic polarization at 0.96 V in the gaseous product distribution formed at -1.24 V. The electrochemical procedure comprises two polarizations at -1.24 V (1st and 2nd), interspersed by an anodic polarization at 0.96 V.

anionic ligand (Cl⁻ or SO₄²⁻) in a Cu(N3-type) complex has a discrete effect under $g_{||}$ value, but an expressive one on $A_{||}$. That is clear comparing $[Cu(bzimpy)Cl_2]$ from our work $(A_{||}$ = 489) and $[Cu(bzimpy)(H_2O)_2]^{2+}(CF_3SO_3^{-})_2$ from literature $(A_{\parallel} = 372)$. The same appears to be true for the interaction with SO_4^{2-} , which was reported as the probable origin of the expressive value of A_{11} observed for the reaction of $[Cu(BPA)(H_2O)_2]^{2+}$ complex with $SO_4^{2-.61}$ In our work, the electrochemical reduction of the copper center in [Cu-(bzimpy)Cl₂] during ERCO₂ must readily promote the labialization of Cl⁻ ligand. The posterior anodic oxidation of the copper center certainly must not regenerate the Cloriginal complexes. Still, the moiety [CuN3] (N3 = bzimpy) might be formed and converted to a geometrically similar species containing a different ligand. Here, the sulfate anion rises as a good guess, since the electrolysis is performed in K_2SO_4 (0.1 mol L^{-1}), and SO_4^{2-} can bind to metals in a bidentate mode. Therefore, the $SO_4^{\ 2-}$ binding to [CuN3] would agree with the larger $A_{\parallel} = 535$ value for [Cu(bzimpy)-Cl₂]* (postanodic sample) when compared to [Cu(bzimpy)- $(L)_2$ (L = Cl⁻ and H_2O), A_{\parallel} = 489 and 372, respectively.

In parallel, post-ERCO₂ and anodic polarization at 0.96 V using $[Cu(pyrben)_2(NO_3)]NO_3$ as precatalysts did not produce an evident Cu^{2+} EPR signal, Figure 5d. These results may indicate that the $[Cu(pyrben)_2(NO_3)]NO_3$ complex is less stable and more susceptible to Cu^{2+} dissolution after ERCO₂ and anodic polarization. Such behavior agrees with the quantitative analysis performed by GC and presented next.

The XAS and EPR results revealed important information concerning the identity of the species formed at -1.24 and 0.96 V. Next, the effects of the induced restructuring of the Cu complexes on their catalytic performance will be presented. The quantitative GC results, depicted in Figure 6, show that during the first polarization at -1.24 V, all catalysts but $CuCO_3.Cu(OH)_2$ exhibit higher selectivity toward ERCO $_2$. However, after holding the potential at 0.96 V, the scenario drastically changes based on the identity of the Cu-based

material: while $[Cu(bzimpy)Cl_2]$ shows slight changes in product distribution, both $[Cu(pyrben)_2(NO_3)]NO_3$ and $CuCO_3.Cu(OH)_2$ exhibit a significant enhancement of the HER, an increase in CO formation, and a suppression in ethylene formation. In the EC-MS experiments (Figure S22), the same trends were observed. Note, however, that the ion current of m/z fragment 28 (CO) decreases after anodic polarization, which is reasonable since such a fragment also comes from ethylene. These results evidence that $[Cu-(bzimpy)Cl_2]$ is the only catalyst that keeps similar selectivity before and after polarization at 0.96 V, which would be expected in a partially reversible restructuring.

By analyzing the current densities before and after anodic polarization (Figure S23) a significant current drop is observed for all catalysts, which is possibly related to the diffusion of Cu^{2+} into the electrolyte. However, compared to [Cu-(pyrben)₂(NO₃)]NO₃ and CuCO₃.Cu(OH)₂, [Cu(bzimpy)-Cl₂] exhibited the highest current density after anodic polarization, most of which is directed to ERCO₂ (as shown in Figure 6). Therefore, the loss of Cu^{2+} may be less pronounced for [Cu(bzimpy)Cl₂] than for the other two catalysts.

The results presented so far indicate that *bzimpy* plays an important role in maintaining copper on the electrode surface after anodic polarization, which is likely achieved through the coordination of Cu²⁺ to the ligand. We then hypothesize that this property of *bzimpy* comes from its tridentate structure, making it more effective in immediately coordinating to aqueous Cu²⁺ ions formed after anodic polarization. It is worth mentioning, however, that the observed restructuring of [Cu(bzimpy)Cl₂] cannot be considered a completely reversible process, given that a fraction of the Cu²⁺ diffuses into the electrolyte and that the structure of the complex formed at 0.96 V would present new groups replacing the original Cl⁻ ligands. Nevertheless, the observed EPR spectrum and calculated parameters remain typical of a square-based pyramidal copper(II) geometry, which agrees with the

presence of the *bzimpy* ligand. In such a species, the marked increase in the $A_{||}$ value is probably due to the stronger interaction with a new ligand, like the $SO_4^{\ 2^-}$ ion, abundantly available under our experimental conditions.

CONCLUSIONS

The present study provides a comprehensive evaluation of the restructuring of copper complexes during the electrochemical reduction of CO₂ in an acidic medium. It was demonstrated that both [Cu(bzimpy)Cl₂] and [Cu(pyrben)₂(NO₃)]NO₃ undergo potential-induced structural changes, where Cu oxidation state and coordination environment dynamically evolve during ERCO₂ from a molecular Cu²⁺/Cu⁺ structure to a nanostructured one. A high Faradaic efficiency toward C2 products (~45%) was obtained at -1.24 V, which was assigned to the formation of undercoordinated Cu⁰ species showing the (100) as the dominant facet. After ERCO₂ and anodic polarization, [Cu(bzimpy)Cl₂] exhibited a partially reversible restructuring, regenerating the main complex moiety, [Cu(bzimpy)]²⁺, as well as the square-based geometry, as suggested by EPR spectroscopy. The findings underscore the central role of the ligand structure on the complex's catalytic properties, providing insights into the design of nextgeneration molecular copper electrocatalysts for CO2 reduction and highlighting benzimidazole ligands as promising platforms.

■ EXPERIMENTAL SECTION

All chemicals were used as received. A list of all materials and chemicals used in this study is provided in Supplementary Note 1 in the Supporting Information.

Synthesis and Characterization of the Copper Complexes. The synthesis of [Cu(bzimpy)Cl₂] was performed according to the procedure described by Kirpik et al., with minor modifications. [Cu(pyrben)₂(NO₃)]NO₃ was synthesized according to the methodology reported by Butcher and co-workers. Briefly, both complexes were prepared by adding a copper salt in a refluxing methanolic solution of the respective ligand, and their purification were made through recrystallization. A detailed description of the synthesis and purification procedures is provided in Supplementary Note 2 in the Supporting Information.

The structure and purity of both complexes were confirmed through different characterization techniques, as described below. Thermogravimetric analysis (TGA) was performed from 30 to 1000 °C at 10 °C min $^{-1}$, in synthetic air, using a Mettler Toledo (TGA/DSC 2) equipment. Elemental analysis of carbon, hydrogen, and nitrogen was made using a Thermoscientific (FlashSmart) equipment. The X-band (\sim 9.6 GHz) electron paramagnetic resonance (EPR) analysis was performed using a Bruker EMX spectrometer operating at 100 kHz modulation frequency. The results, shown in Figures S1 and S3, and Table S1, are in good agreement with data found in the literature.

Electrochemical Measurements. Electrochemical measurements were performed using an Autolab PGSTAT30 potentiostat or a BioLogic VSP300 potentiostat. CO_2 reduction experiments were conducted in a 0.1 mol L^{-1} K_2SO_4 aqueous solution, which was presaturated with CO_2 for 30 min prior to any measurement (pH = 4.2 after CO_2 saturation). During measurements, CO_2 was continuously purged into the electrolyte. An Ag/AgCl (saturated KCl)

electrode was used as reference electrode. All potential values are referred to the Reversible Hydrogen Electrode (RHE) scale, unless otherwise specified. The conversion from Ag/AgCl to RHE scale was made through the equation $E_{(RHE)} = E_{(Ag/AgCl)} + 0.059 pH + E^{o}_{(Ag/AgCl)}$. iR compensation was used in all measurements (unless otherwise stated), compensating for 85% of the resistance determined by Electrochemical Impedance Spectroscopy. Current values are normalized by the geometric area of the working electrode (WE).

In this study, a total of four different electrochemical cells were used: (a) conventional three-electrodes glass cell for lead underpotential deposition (Pb-UPD) experiments; (b) homemade cylindrical-shaped glass cell for EC-MS measurements; (c) homemade gastight glass cell for GC analysis; and (d) homemade acrylic plastic cell for XAS measurements. A detailed description of each experimental setup, electrode preparation, and cell assembly is provided in the following sections and in the Supporting Information.

Catalysts and Inks Preparation. The catalysts were prepared by grinding the copper-based material with Vulcan carbon using an agate mortar. In all cases, a w/w% (Cumaterial/vulcan) proportion was considered (Table S6). The catalyst ink was then prepared by mixing 1.0 mg of the Cumaterial/vulcan mixture, 490 μ L of acetone (or isopropyl alcohol), and 10 μ L of Nafion solution 5 wt % under sonication, resulting in a catalyst concentration of 2.0 mg mL⁻¹. A fraction of the ink was then drop-casted on a conductive support. The catalyst load and the nature of the conductive support vary according to the experiment, as will be described in the following sections.

Qualitative Analysis by Online Electrochemical Mass Spectrometry (EC-MS). Online EC-MS analysis was performed using an OmniStar GSD320 (Pfeiffer Vacuum) gas analyzer equipped with a stainless-steel capillary probe (0.125 mm inner diameter) and controlled by the QUADERA 4.00 software. The equipment was set to follow the m/z (mass/charge) fragments 2, 15, 26, 28, and 44, resulting from the fragmentation of hydrogen (H_2), methane (CH_4), ethylene (C_2H_4), carbon monoxide (CO_2), respectively. The software was set to record the ion current versus time and applied potential.

The interface between the mass spectrometer and the electrochemical cell was adapted to allow a fast and online detection of the ERCO2 products. The assembly of such an interface is shown in Figure S7 and described in Supplementary Note 3 in the Supporting Information. The electrochemical cell was filled with 15 mL of a 0.1 mol L⁻¹ K₂SO₄ solution (continuously purged with CO₂), and a graphite rod and an Ag/AgCl (sat. KCl) electrode were used as counter and reference electrodes, respectively. The working electrode was a disk-shaped carbon paper (E-TEK, 50% wetproof, 110 µm thickness and 10 mm diameter) pressed against a PTFE membrane (Gore-Tex, 50 μ m thickness and 0.02 μ m pore size), prepared by applying 1.0 ton/cm² for 1 min. The carbon paper was covered with the catalyst by drop-casting the catalyst ink in a total volume of 50 μL . The area of the WE exposed to the electrolyte was 0.38 cm².

Product Quantification. Gas products generated during constant potential electrolysis were quantified through gas chromatography using an Agilent 8860 gas chromatograph equipped with a thermal conductivity detector (TCD) and a flame ionization detector (FID). The GC was also equipped with a secondary valve to divert the CO₂ from the methanizer.

Both CarboPLOT P7 and HP-PLOT/Q columns were used, with argon as the carrier gas. The reaction samples were collected in 0.6 L commercial bags (Tedlar PLV gas sampling bags) and injected into the GC column using a gastight syringe (Hamilton, 25 mL). The quantification was performed using calibration curves (Figure S24), prepared through dilution (in CO₂) of a standard gas mixture containing H₂, CO, CO₂, CH₄, C₂H₆, C₂H₄, and C₂H₂ balanced with argon. Gas sampling bags, gastight syringes, and a digital mass flow controller (AALBORG, GFC17) were used to prepare the calibration curves. The Faradaic Efficiency (FE) of each product was calculated from eq 1:

$$FE = \frac{Fxne^{-}xM}{Q} \tag{1}$$

where F is the Faraday Constant (96485 C mol⁻¹), **ne**⁻ the number of electrons needed to generate a product, **M** is the moles of the product formed during the electrolysis, and **Q** is the electrolysis charge.

Liquid products generated during constant potential electrolysis were quantified through high-performance liquid chromatography using a Shimadzu Prominence UFLC HPLC system equipped with a refractive index detector (RID, RID-10A), an UV—vis absorption detector (SPD-20A, set at 210 nm) and a Bio-Rad Aminex HPX-87H column (set at 40 °C). The mobile phase was a 3.33 mmol L $^{-1}$ H $_2$ SO $_4$ solution, with a 0.6 mL min $^{-1}$ flow rate. The loop volume was 50 μ L. Samples of the electrolyte were collected at specific times and then injected into the HPLC column. Calibration curves for HCOOH, C $_2$ H $_3$ OH, and CH $_3$ COOH (Figure S24) were prepared for product quantification. The FE of each product was also calculated from eq 1.

CO₂ reduction experiments were performed in a homemade gastight glass cell, equipped with a PTFE cap containing an entrance for two electrodes (working and reference) and tubes for gas inlet/outlet. The cell also had an opening on its side, with PTFE locks and O-rings, to insert the counter electrode (Figure S9). A volume of 25 mL (or 10 mL, for HPLC analysis) of 0.1 mol L⁻¹ K₂SO₄ solution was used as electrolyte, which was continuously stirred and purged with CO₂ at a flow rate of 10 mL min⁻¹. Before each electrolysis, the electrolyte was presaturated with CO₂ for 30 min. The reference electrode was an Ag/AgCl (sat. KCl) electrode, and the counter electrode was a disk-shaped carbon tissue, 30 mm in diameter, covered with Pt/C at a platinum load of 0.4 mg cm⁻². The carbon tissue was pressed against a Nafion 117 membrane and then coupled to the electrochemical cell with the Nafion membrane facing the electrolyte. The electrical contact was made through a platinum wire that was not exposed to the electrolyte. The counter electrode compartment was continuously filled with H₂ at a flow rate of 1.0 mL min⁻¹. Such a low flow rate is important to prevent significant H2 crossover through the Nafion membrane. The working electrode was a disk-shaped glassy carbon, 9.0 mm diameter, which was fully covered with the catalyst by drop-casting the catalyst ink in a total volume of 41.2 μ L. A freshly prepared electrode was used for each studied potential.

Most of the quantitative analysis was performed during constant potential electrolysis for 30 min, with all the effluent gas being accumulated in gas sampling bags during the final 20 min of reaction. In stability experiments, the effluent gas was accumulated in specific periods. *iR* compensation was applied in all quantitative measurements.

Lead Underpotential Deposition (Pb-UPD) Experiments. Pb-UPD experiments were performed in a conventional three-electrodes glass cell. The electrolyte was an aqueous solution containing 0.1 mol L^{-1} HClO₄, 1 mmol L^{-1} Pb²⁺ (from PbO) and 1 mmol L^{-1} NaCl. Prior to the measurements, the electrolyte was saturated with argon for at least 1 h. A platinum foil and an Ag/AgCl (sat. KCl) electrode were used as counter and reference electrodes, respectively. Cyclic voltammetry measurements were performed from -0.4 to -0.1 V vs Ag/AgCl at a scan rate of 5 mV s⁻¹. The contact of the WE with the electrolyte was made at -0.2 V vs Ag/AgCl. 50,51,66

Post-ERCO₂ electrodes were characterized by Pb-UPD. Briefly, $\rm CO_2$ reduction was performed in a $\rm CO_2$ -saturated 0.1 mol $\rm L^{-1}$ $\rm K_2SO_4$ solution at $\rm -1.24$ V vs RHE for 30 min. Then, the electrode was transferred (through an argon chamber) to a secondary electrochemical cell to perform the Pb-UPD measurements as described above. The results were compared to the Pb-UPD profile obtained with copper single crystals ((111), (110), and (100)). The preparation of the Cu single crystals is described in Supplementary Note 4 in the Supporting Information.

In Situ X-ray Absorption Spectroscopy (XAS) Measurements. In situ XAS experiments were performed at the ISS (Inner-Shell Spectroscopy) beamline, National Synchrotron Light Source II, Brookhaven National Laboratory. All measurements were performed at the copper K-edge and in fluorescence mode. XAS spectra were acquired during constant potential electrolysis at different potentials, after 30 min of polarization. For both complexes and CuCO₃.Cu(OH)₂, five electrochemical conditions were explored: (a) open circuit potential, (b) 0.16 V, (c) −0.54 V, (d) −1.24 V, and (e) 0.96 V vs RHE. For each condition, iR compensation was applied (85%), and at least 50 spectra were acquired. XAS data were processed using Athena and Artemis software packages.⁶⁷ The input files for the fittings of [Cu(bzimpy)Cl₂] and [Cu-(pyrben)₂(NO₃)]NO₃ used in Artemis were generated based on the crystallographic data reported in literature. 28,29 The passive electron reduction factors (S_0^2) for the catalysts were obtained by the fittings of their EXAFS spectra in the OCP conditions and were used for the fitting analysis of other EXAFS spectra measured with applied potentials.

 ${\rm CO_2}$ reduction experiments were conducted using a custom-designed acrylic plastic electrochemical cell showing a Kapton tape window, ⁶⁸ allowing the X-ray beam to reach the WE surface. The cell was filled with 30 mL of a 0.1 mol L⁻¹ K₂SO₄ solution, which was continuously purged with ${\rm CO_2}$ during the measurements. Before the electrolysis, the electrolyte was purged with ${\rm CO_2}$ for at least 30 min. An Ag/AgCl electrode and a platinum foil were used as reference and counter electrodes, respectively. Carbon paper strips (1 × 2 cm, Toray, 30% wet-proof, 0.3 mm thickness) were used as working electrodes. A round-shaped area of 5 mm diameter was covered with the catalyst, resulting in a catalyst load of 5 mg cm⁻². In this case, the catalyst ink was prepared at a concentration of 4 mg mL⁻¹.

Electron Paramagnetic Resonance (EPR) Experiments. The X-band (~ 9.6 GHz) EPR spectra were recorded in solid state and DMF frozen solution at liquid nitrogen (~ 77 K) and room temperature on a Bruker EMX spectrometer operating at 100 kHz modulation frequency and microwave power of 6.33 mW for powder and 1.0 mW for frozen solution

samples. The spectra were simulated by applying the EasySpin toolbox in Matlab.

 ${\sf Post\text{-}ERCO_2}$ catalyst samples were carefully collected from the dried surface of the glassy carbon electrode and transferred to a 4 mm quartz EPR tube.

Transmission Electron Microscopy Characterization. Cu^0 nanostructures formed from the copper complexes under CO_2 reduction working conditions were characterized by TEM using a FEI TECNAI G^2 F20 microscope at an accelerating voltage of 200 kV. The images were acquired in the High-Angle Annular Dark-Field (HAADF) mode. The sample preparation was performed as follows: at first, the post-ERCO₂ electrode was gently rinsed with water to remove the excess of electrolyte. Then, a gold grid was placed on the electrode surface and gently pressed against it using a glass slide. Finally, the grid was transferred to a glass vial, which was kept under vacuum for at least 3 h.

ASSOCIATED CONTENT

Data Availability Statement

All data are available in the main text or the Supporting Information.

Supporting Information

The Supporting Information is available free of charge at https://pubs.acs.org/doi/10.1021/acscatal.5c06128.

TGA curves, molecular structures of the Cu complexes, cell design details, experimental and simulated EPR results, TEM characterization, FT-EXAFS fitting results, chronoamperometric curves, Pb-UPD characterization, EC-MS results, and calibration curves (PDF)

AUTHOR INFORMATION

Corresponding Authors

Kotaro Sasaki — Chemistry Department, Brookhaven National Laboratory, Upton, New York 11973, United States; orcid.org/0000-0003-2474-8323; Email: ksasaki@bnl.gov

Fabio H. B. Lima — São Carlos Institute of Chemistry, University of São Paulo, São Carlos, SP 13560-970, Brazil; oorcid.org/0000-0001-5501-2429; Email: fabiohbl@iqsc.usp.br

Authors

Rafael L. Romano — São Carlos Institute of Chemistry, University of São Paulo, São Carlos, SP 13560-970, Brazil Maykon L. Souza — São Carlos Institute of Chemistry, University of São Paulo, São Carlos, SP 13560-970, Brazil Antonio C. Roveda, Jr. — São Carlos Institute of Chemistry, University of São Paulo, São Carlos, SP 13560-970, Brazil; orcid.org/0000-0001-9409-8093

Xueru Zhao – Chemistry Department, Brookhaven National Laboratory, Upton, New York 11973, United States

Complete contact information is available at: https://pubs.acs.org/10.1021/acscatal.5c06128

Funding

The Article Processing Charge for the publication of this research was funded by the Coordenacao de Aperfeicoamento de Pessoal de Nivel Superior (CAPES), Brazil (ROR identifier: 00x0ma614).

Notes

The authors declare no competing financial interest.

ACKNOWLEDGMENTS

The authors acknowledge the financial support from São Paulo Research Foundation (FAPESP), Conselho Nacional de Desenvolvimento Científico e Tecnológico (CNPq), and Coordenação de Aperfeiçoamento de Pessoal de Nível Superior (CAPES). R.L.R. acknowledges FAPESP (#2021/ 03263-9 and #2023/11453-8) and CNPq (#140014/2021-7) for the scholarships. A.C.R.Jr also acknowledges FAPESP (#2021/13985-1) for the scholarship. F.H.B.L. acknowledges FAPESP (Thematic project #2019/22183-6) and CNPq (#308948/2022-0 and 406933/2021-9). F.H.B.L. also acknowledge RCGI (Research Centre for Greenhouse Gas Innovation) hosted by the University of Sao Paulo (USP) and sponsored by FAPESP 2014/50279-4 and 2020/15230-5, and the strategic importance of the support given by ANP -Brazil's National Oil, Natural Gas and Biofuels Agency, through the R&D levy regulation. The authors thank the Laboratory of Structural Characterization (LCE/DEMa/ UFSCar) for the general facilities. This research used resources of the ISS (Inner-Shell Spectroscopy) beamline of the National Synchrotron Light Source II, a U.S. Department of Energy (DOE) Office of Science User Facility operated for the DOE Office of Science by Brookhaven National Laboratory under Contract No. DE-SC0012704. The authors would like to thank Dr. Anatoly I. Frenkel and Dr. Ryuichi Shimogawa from Brookhaven National Laboratory for the valuable discussion on the EXAFS analysis.

REFERENCES

- (1) Nitopi, S.; et al. Progress and Perspectives of Electrochemical CO₂ Reduction on Copper in Aqueous Electrolyte. *Chem. Rev.* **2019**, 119, 7610–7672.
- (2) Farooqi, S. A.; Farooqi, A. S.; Sajjad, S.; Yan, C.; Victor, A. B. Electrochemical Reduction of Carbon Dioxide Into Valuable Chemicals: a Review. *Environ. Chem. Lett.* **2023**, *21*, 1515–1553.
- (3) Chang, B.; et al. Electrochemical Reduction of Carbon Dioxide to Multicarbon (C₂₊) Products: Challenges and Perspectives. *Energy Environ. Sci.* **2023**, *16*, 4714–4758.
- (4) Kortlever, R.; Shen, J.; Schouten, K. J. P.; Calle-Vallejo, F.; Koper, M. T. M. Catalysts and Reaction Pathways for the Electrochemical Reduction of Carbon Dioxide. *J. Phys. Chem. Lett.* **2015**, *6*, 4073–4082.
- (5) Garza, A. J.; Bell, A. T.; Head-Gordon, M. Mechanism of CO2 Reduction at Copper Surfaces: Pathways to C2 Products. *ACS Catal.* **2018**, *8*, 1490–1499.
- (6) Chen, C.; Khosrowabadi Kotyk, J. F.; Sheehan, S. W. Progress Toward Commercial Application of Electrochemical Carbon Dioxide Reduction. *Chem.* **2018**, *4*, 2571–2586.
- (7) Hori, Y.; Kikuchi, K.; Suzuki, S. Production of CO and CH4 in Electrochemical Reduction of CO2 at Metal Electrodes in Aqueous Hydrogencarbonate Solution. *Chem. Lett.* **1985**, *14*, 1695–1698.
- (8) Bagger, A.; Ju, W.; Varela, A. S.; Strasser, P.; Rossmeisl, J. Electrochemical CO2 Reduction: A Classification Problem. *Chem-PhysChem* **2017**, *18*, 3266–3273.
- (9) Kim, K.; Wagner, P.; Wagner, K.; Mozer, A. J. Electrochemical CO2 Reduction Catalyzed by Copper Molecular Complexes: The Influence of Ligand Structure. *Energy Fuels* **2022**, *36*, 4653–4676.
- (10) Liang, H. Q.; Beweries, T.; Francke, R.; Beller, M. Molecular Catalysts for the Reductive Homocoupling of CO2 towards C2+Compounds. *Angew. Chem., Int. Ed.* **2022**, *61*, No. e202200723.
- (11) Kim, D.; et al. Acid-Stable Cu Cluster Precatalysts Enable High Energy and Carbon Efficiency in CO₂ Electroreduction. *J. Am. Chem. Soc.* **2024**, *146*, 27701–27712.
- (12) Du, J.; Cheng, B.; Jiang, L.; Han, Z. Copper Phenanthroline for Selective Electrochemical CO2 Reduction on Carbon Paper. *Chem. Commun.* **2023**, *59*, 4778–4781.

- (13) Nam, D. H.; et al. Molecular Enhancement of Heterogeneous CO₂ Reduction. *Nat. Mater.* **2020**, *19*, 266–276.
- (14) Zhao, S.; et al. Steering Carbon Dioxide Reduction Toward C–C Coupling Using Copper Electrodes Modified with Porous Molecular Films. *Nat. Commun.* **2023**, *14*, 844.
- (15) Fan, M.; et al. Single-Site Decorated Copper Enables Energyand Carbon-Efficient CO₂ Methanation in Acidic Conditions. *Nat. Commun.* **2023**, *14*, 3314.
- (16) Zhao, S.; Yang, Y.; Tang, Z. Insight into Structural Evolution, Active Sites, and Stability of Heterogeneous Electrocatalysts. *Angew. Chem., Int. Ed.* **2022**, *61*, No. e202110186.
- (17) Lai, W.; et al. Dynamic Evolution of Active Sites in Electrocatalytic CO₂ Reduction Reaction: Fundamental Understanding and Recent Progress. *Adv. Funct. Mater.* **2022**, 32, No. 2111193.
- (18) Yusuf, B. A.; et al. Insights into the Dynamic Evolution of Catalytic Active Centers of the Electrocatalytic Carbon Dioxide Reduction Reaction. *Coord. Chem. Rev.* **2023**, 492, No. 215273.
- (19) Weng, Z.; et al. Active Sites of Copper-Complex Catalytic Materials for Electrochemical Carbon Dioxide Reduction. *Nat. Commun.* **2018**, *9*, 415.
- (20) Ma, L.; et al. Covalent Triazine Framework Confined Copper Catalysts for Selective Electrochemical CO₂ Reduction: Operando Diagnosis of Active Sites. ACS Catal. **2020**, 10, 4534–4542.
- (21) Popović, S.; et al. Stability and Degradation Mechanisms of Copper-Based Catalysts for Electrochemical CO₂ Reduction. *Angew. Chemie Int. Ed.* **2020**, 59, 14736–14746.
- (22) Dong, Z.; et al. Benzimidazole Modified Nickel Phthalocyanine Effectively Achieves CO₂ to CO Conversion in a Wide pH Range of Aqueous Solutions. *Sep. Purif. Technol.* **2025**, *361*, No. 131367.
- (23) Bengtsson, P.; et al. Molecularly Designed Cathode for Copper-Benzimidazole-Induced CO₂ Reduction to MeOH. *Angew. Chem., Int. Ed.* **2025**, *64*, No. e202504783.
- (24) Paul, L.; Gu, M.; Moise, S.; Harrison, D. P.; Norris, M. R. Six-Electron CO2 Reduction Involving Participation by Benzimidazole-Derived Bidentate Ligands in Ruthenium Complexes. *ACS Appl. Energy Mater.* **2022**, *5*, 9280–9285.
- (25) Pankhurst, J. R.; Guntern, Y. T.; Mensi, M.; Buonsanti, R. Molecular Tunability of Surface-Functionalized Metal Nanocrystals for Selective Electrochemical CO2 Reduction. *Chem. Sci.* **2019**, *10*, 10356–10365.
- (26) Liu, T.; Chen, L.; Chao, D. Noble Metal-Free bis-Tridentate Benzimidazole Zinc(II) and Iron(II) Complexes for Selective CO2 Photoreduction. *Dalt. Trans.* **2022**, *51*, 4052–4057.
- (27) Kırpık, H.; Kose, M. Transition Metal Complexes of a Benzimidazole Ligand Containing Two Heptyl Chains: Synthesis, Crystal Structures, Photophysical and Thermal Properties. *J. Mol. Struct.* **2020**, *1200*, No. 127073.
- (28) Patel, R. N.; et al. Copper(II) Mononuclear Complexes Incorporating Pyridine Derivatives: Synthesis, Structural Characterization, and Unusual X-Band epr Spectra. *J. Chem. Crystallogr.* **2022**, 52, 378–393.
- (29) Bernardinelli, G.; Hopfgartner, G.; Williams, A. F. Structure of [2,6-bis(2-benzimidazolyl)pyridine]dichlorocopper(II) Dimethylformamide. *Acta Crystallogr.* **1990**, *C46*, 1642–1645.
- (30) Altaf, M.; Stoeckli-Evans, H. Nickel(II) and Copper(II) Complexes of 2-(2-pyridyl)benzimidazole: Synthesis and Structural Characterization. *Transit. Met. Chem.* **2009**, *34*, 613–620.
- (31) Lada, Z. G.; et al. Probing the Electronic Structure of a Copper(II) Complex by CW- and Pulse-EPR Spectroscopy. *Dalt. Trans.* **2017**, *46*, 8458–8475.
- (32) Telser, J. A Perspective on Applications of Ligand-Field Analysis: Inspiration from Electron Paramagnetic Resonance Spectroscopy of Coordination Complexes of Transition Metal Ions. *J. Braz. Chem. Soc.* **2006**, *17*, 1501–1515.
- (33) Prosser, K. E.; Walsby, C. J. Electron Paramagnetic Resonance as a Tool for Studying the Mechanisms of Paramagnetic Anticancer Metallodrugs. *Eur. J. Inorg. Chem.* **2017**, 2017, 1573–1585. (2017)

- (34) Neuman, N. I.; et al. Single Crystal EPR of the Mixed-Ligand Complex of Copper(II) with L-Glutamic acid and 1,10-Phenanthroline: A Study on the Narrowing of the Hyperfine Structure by Exchange. *J. Phys. Chem. A* **2012**, *116*, 12314–12320.
- (35) De Medeiros, W. M. T. Q.; et al. A Vanillin-Based Copper(II) Metal Complex with a DNA-Mediated Apoptotic Activity. *RSC Adv.* **2018**, *8*, 16873–16886.
- (36) Maheshwaran, D.; Priyanga, S.; Mayilmurugan, R. Copper(II)-Benzimidazole Complexes as Efficient Fluorescent Probes for L-Cysteine in Water. *Dalt. Trans.* **2017**, *46*, 11408–11417.
- (37) Sohtun, W. P.; Muthuramalingam, S.; Velusamy, M.; Mayilmurugan, R. New Class of Tridentate 3N Ligands and Copper(II) Complexes: A Model for Type-2 Copper Site of Phenoxazinone Synthase. *Inorg. Chem. Commun.* **2019**, *110*, No. 107608.
- (38) Beverskog, B.; Puigdomenech, I. Revised Pourbaix Diagrams for Copper at 25 to 300°C. *J. Electrochem. Soc.* **1997**, *144*, 3476–3483.
- (39) González, S.; Pérez, M.; Barrera, M.; González Elipe, A. R.; Souto, R. M. Mechanism of Copper Passivation in Aqueous Sodium Carbonate-Bicarbonate Solution Derived from Combined X-ray Photoelectron Spectroscopic and Electrochemical Data. *J. Phys. Chem. B* 1998, 102, 5483–5489.
- (40) Pérez Sánchez, M.; et al. Electrochemical Behaviour of Copper in Aqueous Moderate Alkaline Media, Containing Sodium Carbonate and Bicarbonate, and Sodium Perchlorate. *Electrochim. Acta* **1990**, 35, 1337–1343.
- (41) Batchelor-McAuley, C. Defining the Onset Potential. *Curr. Opin. Electrochem.* **2023**, *37*, No. 101176.
- (42) Huang, Y.; Handoko, A. D.; Hirunsit, P.; Yeo, B. S. Electrochemical Reduction of CO2 Using Copper Single-Crystal Surfaces: Effects of CO* Coverage on the Selective Formation of Ethylene. *ACS Catal.* **2017**, *7*, 1749–1756.
- (43) Kim, T.; Palmore, G. T. R. A Scalable Method for Preparing Cu Electrocatalysts that Convert CO2 into C2+ Products. *Nat. Commun.* **2020**, *11*, 3622.
- (44) Yang, B.; et al. Electrocatalytic CO₂ Reduction to Alcohols by Modulating the Molecular Geometry and Cu Coordination in Bicentric Copper Complexes. *Nat. Commun.* **2022**, *13*, 5122.
- (45) Liu, C.; et al. pH Variation in the Acidic Electrochemical CO₂ Reduction Process. *Langmuir* **2024**, *40*, 19370.
- (46) Huang, J.; et al. Potential-Induced Nanoclustering of Metallic Catalysts During Electrochemical CO₂ Reduction. *Nat. Commun.* **2018**, *9*, 3117.
- (47) Wuttig, A.; Surendranath, Y. Impurity Ion Complexation Enhances Carbon Dioxide Reduction Catalysis. *ACS Catal.* **2015**, *5*, 4479–4484.
- (48) Lee, S. H.; et al. Correlating Oxidation State and Surface Area to Activity from Operando Studies of Copper CO Electroreduction Catalysts in a Gas-Fed Device. *ACS Catal.* **2020**, *10*, 8000–8011.
- (49) Drisdell, W.; et al. Structural Transformation and Degradation of Cu Nanocatalysts during Electrochemical CO₂ Reduction Reaction. *J. Am. Chem. Soc.* **2025**, *147*, 6536–6548.
- (50) Sebastián-Pascual, P.; Escudero-Escribano, M. Surface Characterization of Copper Electrocatalysts by Lead Underpotential Deposition. *J. Electroanal. Chem.* **2021**, 896, No. 115446.
- (51) Couce, P. M.; et al. Tailoring the Facet Distribution on Copper with Chloride. *Chem. Sci.* **2024**, *15*, 1714–1725.
- (52) Shadle, S. E.; Hodgson, K. O.; Solomon, E. I.; Hedman, B.; Schugar, H. J. X-ray Absorption Spectroscopic Studies of the Blue Copper Site: Metal and Ligand K-Edge Studies To Probe the Origin of the EPR Hyperfine Splitting in Plastocyanin. *J. Am. Chem. Soc.* 1993, 115, 767–776.
- (53) Solomon, E. I.; et al. Copper Active Sites in Biology. *Chem. Rev.* **2014**, *114*, 3659–3853.
- (54) Yano, J.; Yachandra, V. K. X-ray Absorption Spectroscopy. *Photosynth. Res.* **2009**, *102*, 241–254.
- (55) Bairagi, M.; et al. Probing Coordination Geometry and Electronic Nature of Cu Center in Mixed Ligand N, N, N', N'-

- tetramethylethylenediamine Copper Complexes Using XAFS. Radiat. Phys. Chem. 2024, 218, No. 111609.
- (56) Yang, Y.; et al. Operando Studies Reveal Active Cu Nanograins for CO₂ Electroreduction. *Nature* **2023**, *614*, 262–269.
- (57) Jung, H.; et al. Electrochemical Fragmentation of Cu₂O Nanoparticles Enhancing Selective C-C Coupling from CO₂ Reduction Reaction. *J. Am. Chem. Soc.* **2019**, *141*, 4624–4633.
- (58) Duan, G.; et al. Highly Efficient Electrocatalytic CO_2 Reduction to C_{2+} Products on a Poly(ionic liquid)-Based Cu^0-Cu^I Tandem Catalyst. *Angew. Chem.* **2022**, *134*, No. e202110657.
- (59) Sasaki, K.; Marinkovic, N.; Isaacs, H. S.; Adzic, R. R. Synchrotron-Based in Situ Characterization of Carbon-Supported Platinum and Platinum Monolayer Electrocatalysts. *ACS Catal.* **2016**, *6*, 69–76.
- (60) Hoffmann, S. K.; Goslar, J.; Ratajczak, I.; Mazela, B. Fixation of Copper-Protein Formulation in Wood: Part 2. Molecular Mechanism of Fixation of Copper(II) in Cellulose, Lignin and Wood Studied by EPR. *Holzforschung* **2008**, *62*, 300–308.
- (61) Spencer, J.; Stevens, J.; Perry, C.; Murphy, D. M. An EPR Investigation of Binding Environments by N-Donor Chelating Exchange Resins for Cu Extraction from Aqueous Media. *Inorg. Chem.* **2018**, *57*, 10857–10866.
- (62) Machura, B.; Świtlicka, A.; Wolff, M.; Kusz, J.; Kruszynski, R. Synthesis, Spectroscopic Characterization, X-ray Structure and DFT Calculations of Copper(II) Complex with 2-(2-pyridyl)-benzimidazole. *Polyhedron* **2009**, 28, 1348–1354.
- (63) Machura, B.; Świtlicka, A.; Penkala, M. N- and S-Bonded Thiocyanate Copper(II) Complexes of 2,6-bis-(benzimidazolyl)-pyridine Synthesis, Spectroscopic Characterization, X-ray Structure and DFT calculations. *Polyhedron* **2012**, *45*, 221–228.
- (64) Kauffman, D. R.; et al. Selective Electrocatalytic Reduction of CO₂ into CO at Small, Thiol-Capped Au/Cu Nanoparticles. *J. Phys. Chem. C* **2018**, 122, 27991–28000.
- (65) Souza, M. L.; Lima, F. H. B. Dibenzyldithiocarbamate-Functionalized Small Gold Nanoparticles as Selective Catalysts for the Electrochemical Reduction of CO2 to CO. *ACS Catal.* **2021**, *11*, 12208–12219.
- (66) Wu, D.; et al. Electroless Deposition of Pb Monolayer: A New Process and Application to Surface Selective Atomic Layer Deposition. *Langmuir* **2018**, 34, 11384–11394.
- (67) Ravel, B.; Newville, M. ATHENA, ARTEMIS, HEPHAESTUS: Data Analysis for X-ray Absorption Spectroscopy Using IFEFFIT. *J. Synchrotron Radiat.* **2005**, *12*, 537–541.
- (68) Han, X.; et al. Theoretical Prediction and Experimental Verification of IrOx Supported on Titanium Nitride for Acidic Oxygen Evolution Reaction. J. Am. Chem. Soc. 2024, 146, 16499—16510

